Supporting Information

Resolving the ultrafast dynamics of the anionic green fluorescent protein chromophore in water

Chey M. Jones,[1,2] Nanna H. List,[1,2] and Todd J. Martínez[1,2,*]

[1]Department of Chemistry and The PULSE Institute, Stanford University, Stanford, CA 94305
[2]SLAC National Accelerator Laboratory, 2575 Sand Hill Road, Menlo Park, CA 94025

Table of Contents

I. Validation of α-CASSCF

Prior to running our nonadiabatic dynamics simulations, we benchmarked the validity of α-CASSCF based on reference XMS-CASPT2 calculations. After choosing an α parameter in optimal agreement with the S_0/S_1 energy gap of XMS-CASPT2 at the Franck-Condon (FC) point, the qualitative and quantitative aspects of α-CASSCF were evaluated. As seen in Figure S1, using an α correction for the solvated system is beneficial for describing the potential energy surface (PES) topology of the ground and excited states. Using α(0.67)-SA3-CASSCF(4,3)/6-31G* with a D3 dispersion correction, geometries along characteristic ϕ_I- and ϕ_P-twisted dihedrals produce a PES with the same qualitative features as XMS-CASPT2. Most notably, the energetic gradient of SA3-CASSCF(4,3) on S_1 appears much steeper (after 30° rotation along ϕ_I or ϕ_P) than that of α(0.67)-SA3-CASSCF(4,3) and XMS-CASPT2, which may artificially accelerate excited-state dynamics. Quantitatively, α-CASSCF predicts electronic state energies that are much closer to XMS-CASPT2 values than SA3-CASSCF for these geometries. Critical points for the QM/MM system were obtained using the same partitioning scheme described for the QM/MM-MD, treating the chromophore at the α(0.67)-SA3-CASSCF(4,3)/6-31G* level. Optimized geometries along ϕ_I- and ϕ_P-twisting pathways were reached by coordinate driving along the respective dihedral, keeping the other dihedral angle fixed at zero degrees and allowing all other degrees of freedom to relax. I- and P-twisted minimum energy conical intersections (MECIs) were reached by initiating an MECI search from the 90° I- and P-twisted minima, respectively.

Although MECIs do not necessarily reflect geometries that are encountered during the dynamics, they can provide useful information about notable geometric features of the PES. It is known that $HBDI^-$ has two primary MECIs in water: one dominated by torsion along ϕ_I and the other dominated by torsion along ϕ_P.[1] For our explicitly-solvated systems, these conical intersections are encountered with α-CASSCF (Figure S2). Associated with these MECIs are characteristic geometric features (Table S1). In the case of the I-twisted MECI (MECI-I), degeneracy between the ground and excited states is achieved by rotation along ϕ_I with little pyramidalization of the bridge carbon. Additionally, the bridge bond closer to the I-ring (r_I) is considerably longer than the bridge bond closer to the P-ring (r_P). For the P-twisted MECI (MECI-P), this relationship between the bridge bond lengths is reversed and the pyramidalization

requirement increases by more than a factor of two. Reaching the MECI-P also requires non-negligible twisting along ϕ_I, making the structure less dominated by a single rotation than its I-twisted counterpart. Reaching these MECIs through incremental twisting along their respective dihedrals suggests that both MECIs lie below the FC point, consistent with previous claims that solvation permits energetically accessible CIs between the excited state and the ground state.[2, 3]

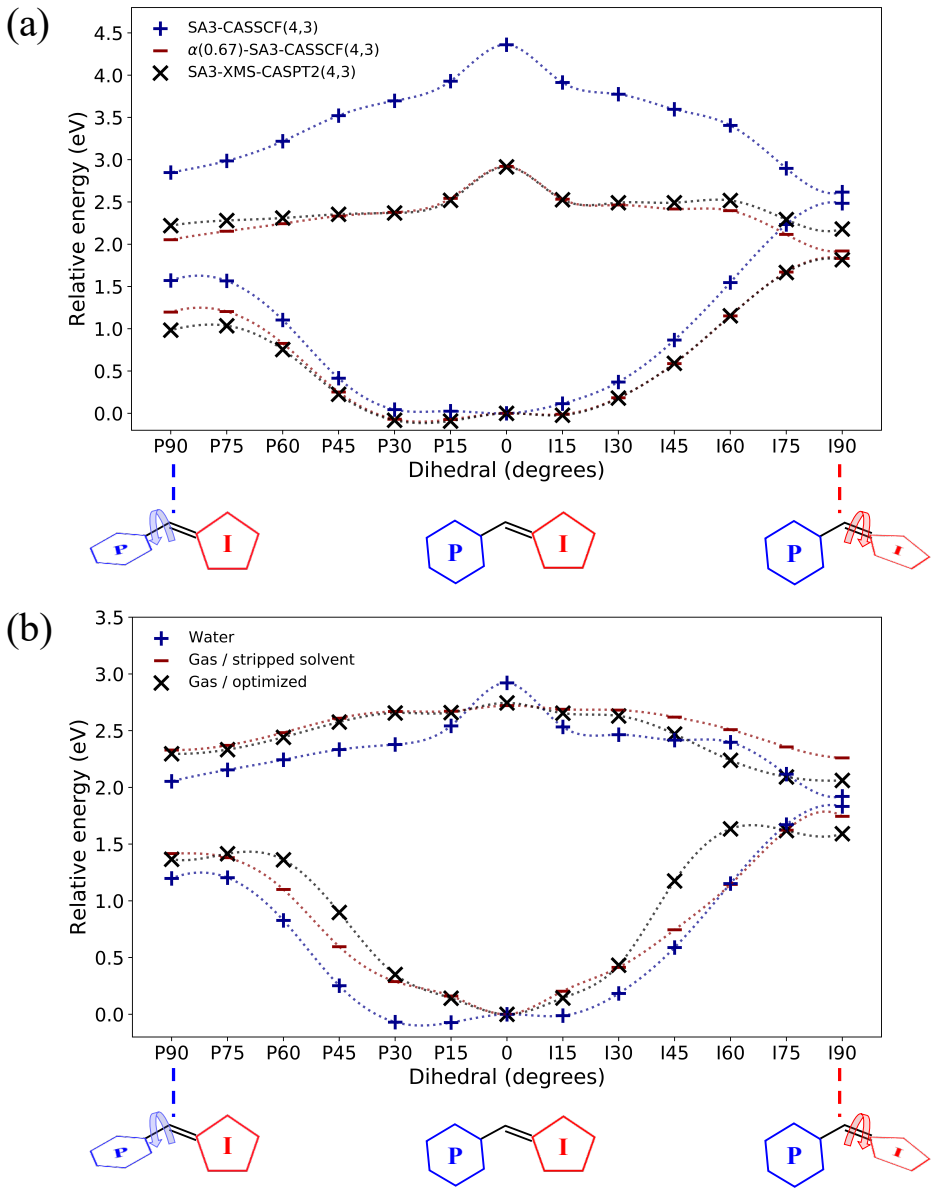

Figure S1: Relative energy comparison for aqueous $HBDI^-$ upon twisting along the ϕ_I and ϕ_P angles. (a) Energies of $HBDI^-$ geometries in explicit water. The planar geometry (labeled as "0") was optimized on S_0 as a reference FC structure. The ϕ_I- and ϕ_P-twisted structures were optimized on S_1 in succession (using 15° intervals and the previous optimized geometry as a starting point) to avoid large disruptions to the local solvent, keeping the non-twisted dihedral angle fixed at 0°. SA3-CASSCF(4,3)/6-31G* and XMS-CASPT2(4,3)/6-31G* energies were computed using single point energy calculations on α(0.67)-SA3-CASSCF(4,3)/6-31G* optimized geometries. (b) Effect of solvent stabilization for non-equilibrated configurations of aqueous $HBDI^-$. Gas-phase energies were derived from single point energy calculations on aqueous $HBDI^-$ geometries in (a), after stripping the solvent. Optimized gas-phase energies are from optimized stripped-solvent geometries. Lower markers represent S_0 energies and upper markers represent S_1 energies. α(0.67)-SA3-CASSCF(4,3)/6-31G* was used for each system.

II. Critical points of aqueous HBDI⁻ using α-CASSCF

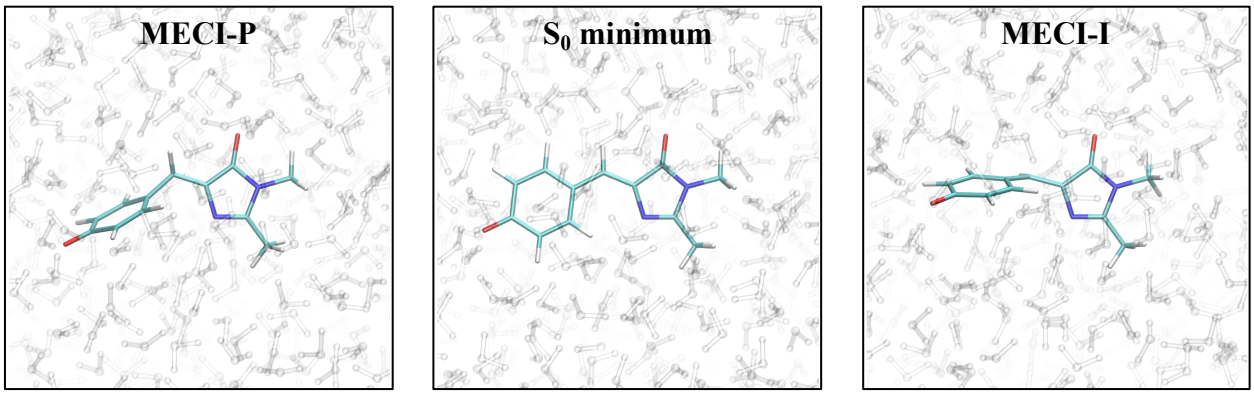

Figure S2: Representative geometries of the ground-state (S_0) minimum and S_0/S_1 MECIs of HBDI⁻ in water treated with α(0.67)-SA3-CASSCF(4,3)/6-31G*.

III. Benchmark of α-CASSCF along an AIMS trajectory

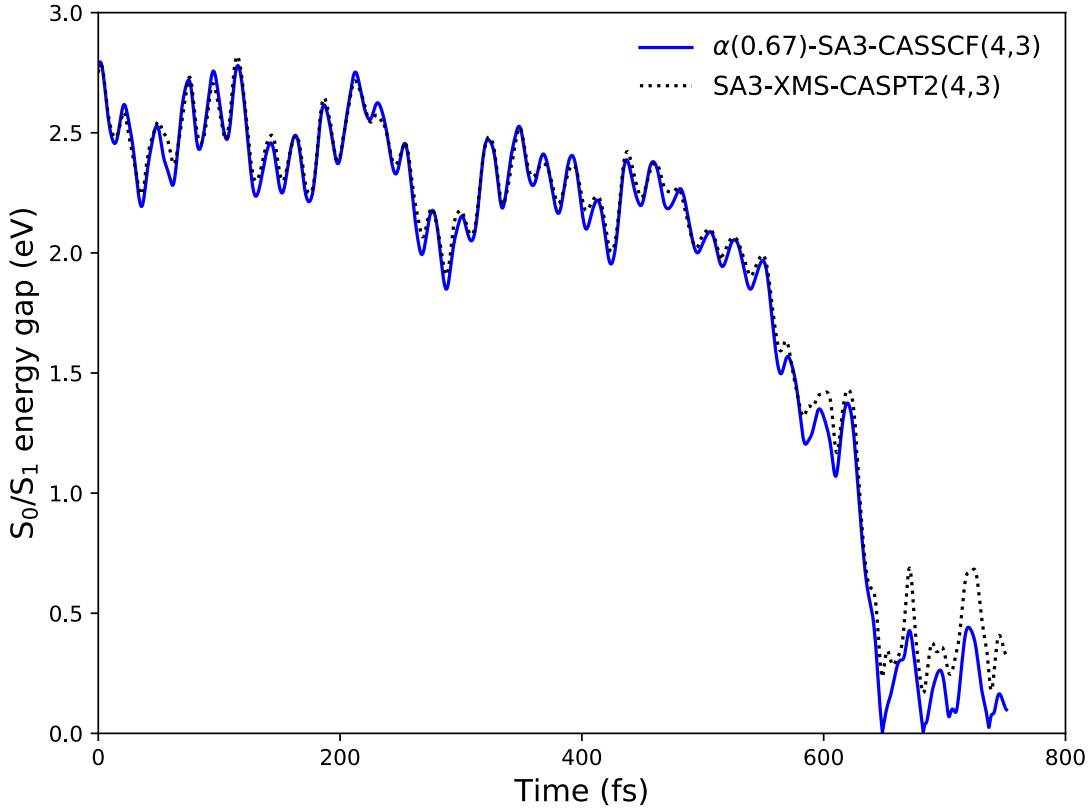

Figure S3: Benchmarked performance of α-CASSCF relative to XMS-CASPT2(4,3) for $HBDI^-$ in water. Energy shown corresponds to the S_0/S_1 energy gap along an I-deactivating α-CASSCF AIMS trajectory. XMS-CASPT2(4,3) energies were computed for each geometry along the AIMS trajectory. The 6-31G* basis set was used for both methods.

IV. Isoenergetic enantiomers of HBDI⁻

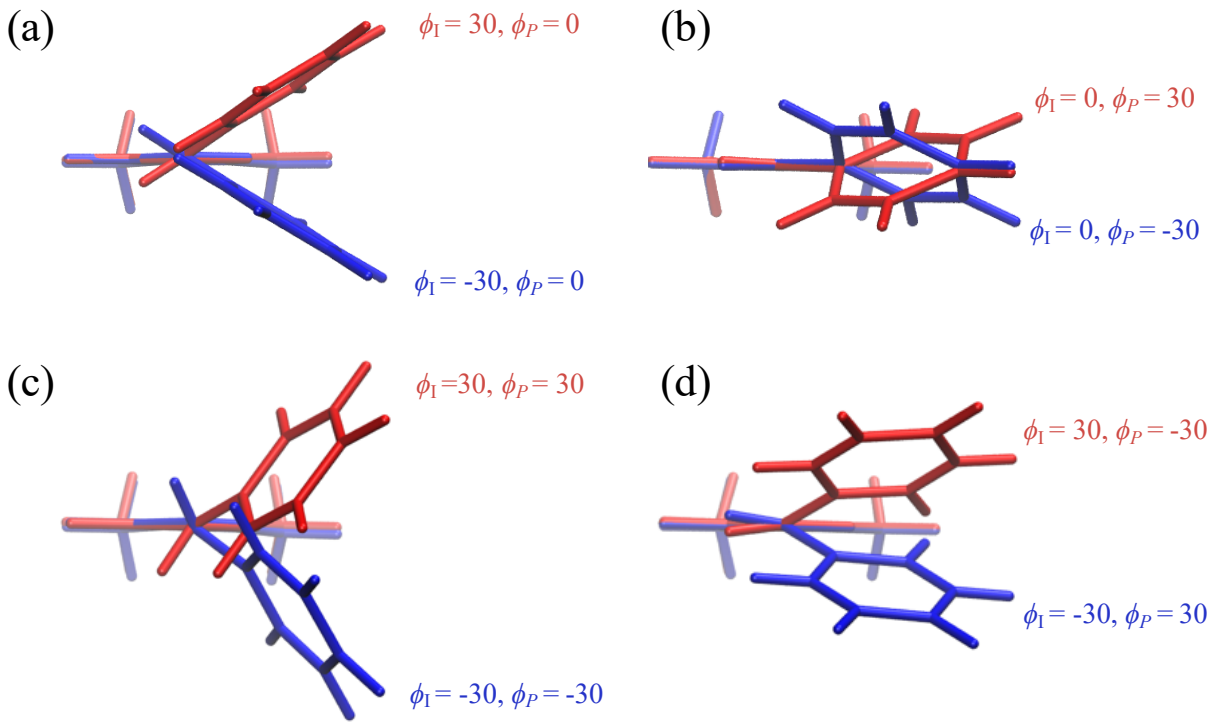

Figure S4: Optimized S_1 geometries of gas-phase HBDI⁻, fixed at specific dihedral angles, to illustrate isoenergetic enantiomers with respect to the ϕ_I and ϕ_P twisting dihedral angles. Geometries were optimized to illustrate symmetry with respect to (a) I-twisting, (b) P-twisting, and (c)-(d) simultaneous I- and P-twisting. Geometries were optimized using α(0.67)-SA3-CASSCF(4,3)/6-31G*.

V. Equilibration of free energy during umbrella sampling

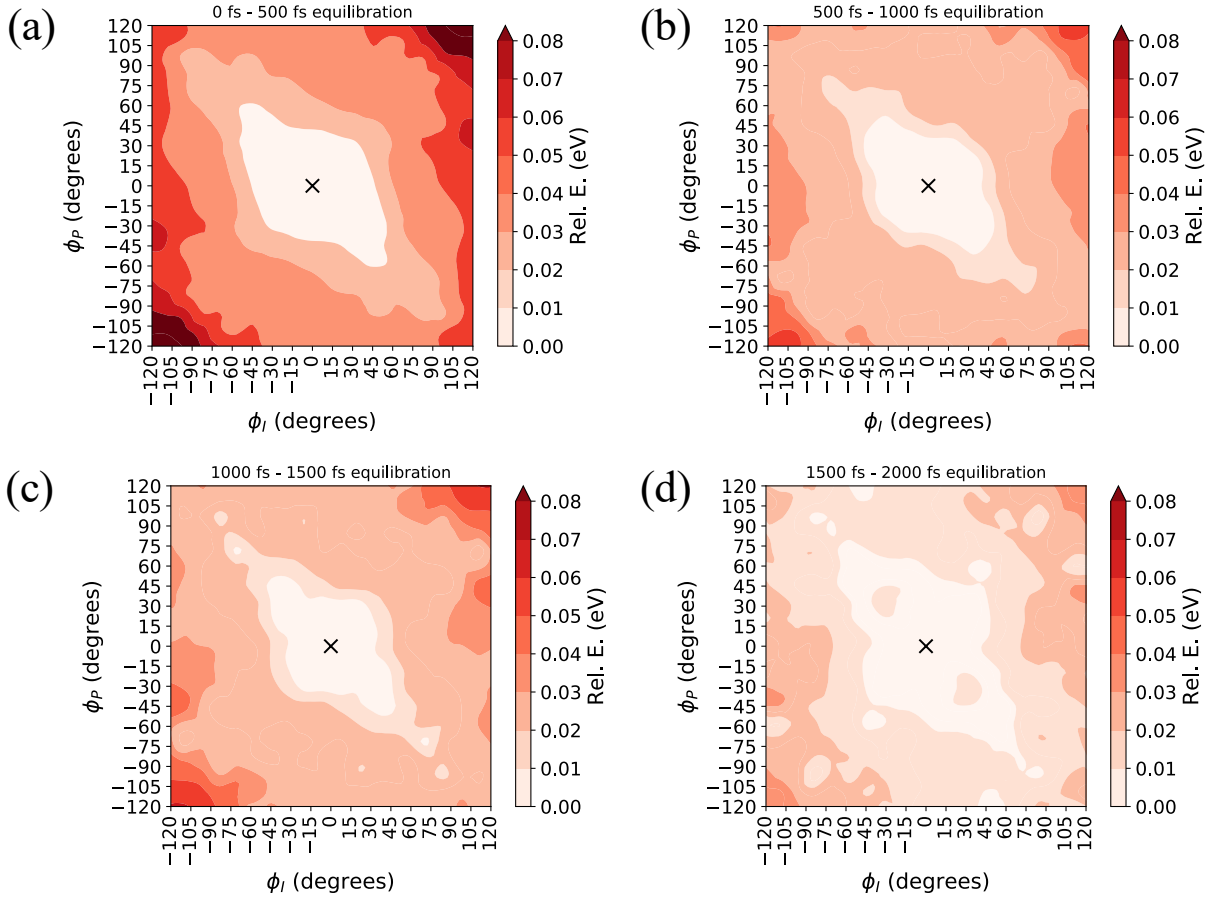

Figure S5: (a)-(d) Potential of mean force (PMF) differences between various time periods during the umbrella sampling of aqueous $HBDI^-$ on S_1. In each panel, the absolute relative free energy difference of the two specified PMFs was taken to estimate the equilibration time for the solvent and chromophore across all windows. Once these fluctuations dropped below 0.05 eV, the system was considered equilibrated.

VI. Fragment-accumulated Mulliken charges across solvated initial conditions

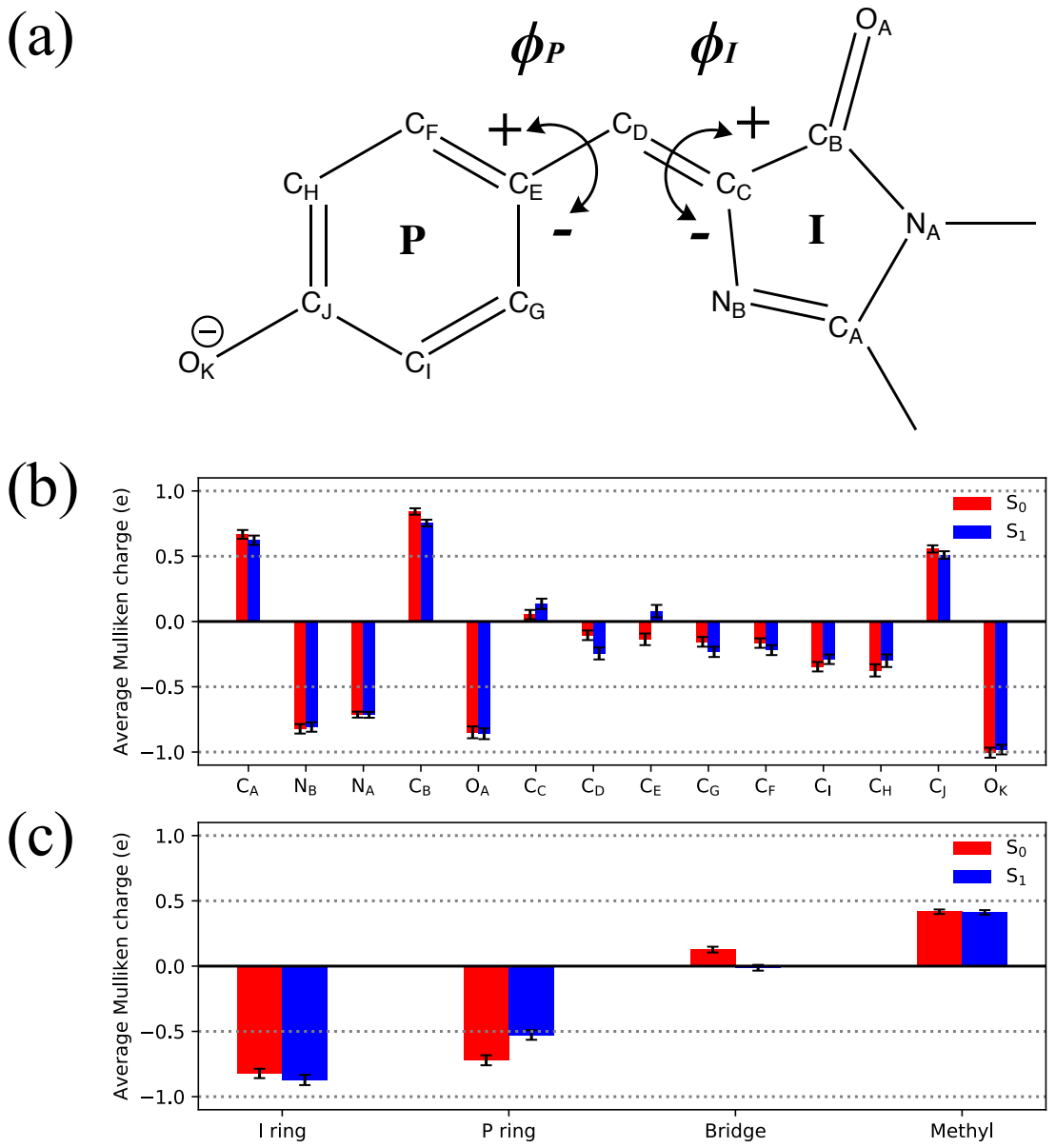

Figure S6: (a) Labeled atoms of $HBDI^-$ with positive and negative dihedral rotations illustrated. Average S_0 and S_1 Mulliken charges localized on (b) atoms and (c) moieties of $HBDI^-$ in water. Average charges were obtained across 500 initial conditions using the α(0.67)-SA3-CASSCF(4,3)/6-31G* level of theory.

VII. Geometric analysis for gas-phase and solvated initial conditions

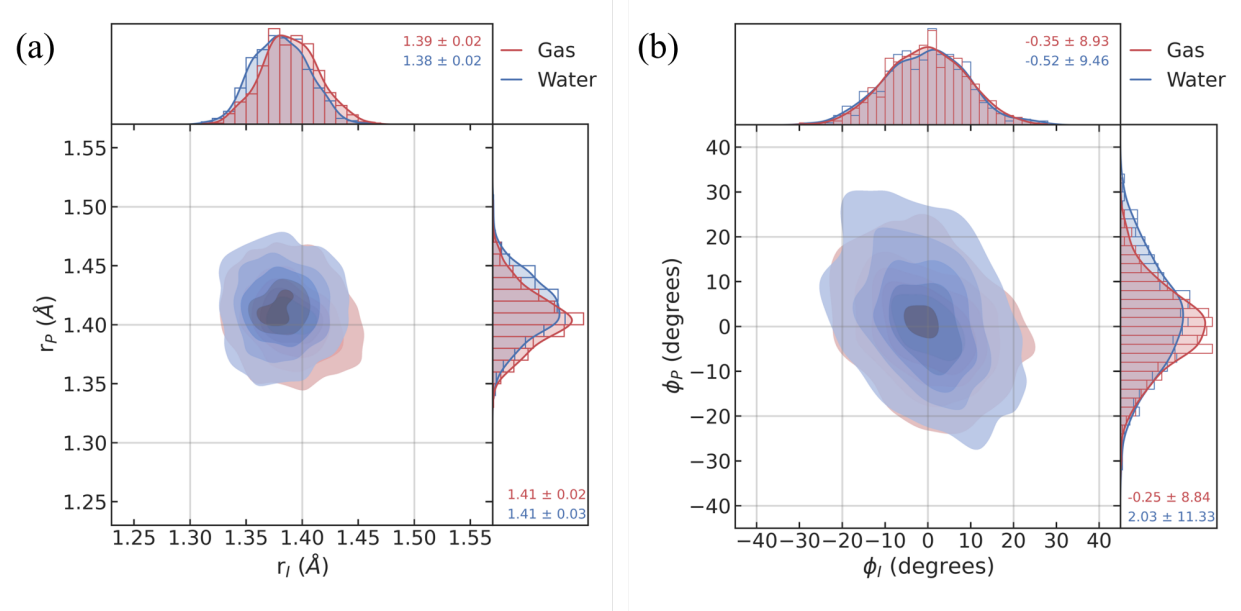

Figure S7: (a) Distributions of carbon-carbon methine bridge bonds adjacent to the imidazolinone (r_I) and phenolate (r_P) rings. (b) Distributions of dihedral angles associated with imidazolinone (ϕ_I) and phenolate (ϕ_P) twisting. Blue indicates data for Boltzmann-sampled initial conditions from aqueous QM/MM-MD simulations at 300K, using α(0.67)-SA3-CASSCF(4,3)/6-31G*. Red indicates data for Boltzmann-sampled initial conditions from a gas-phase QM/MM-MD at 300K, using α(0.64)-SA3-CASSCF(4,3)/6-31G*.

VIII. Geometric analysis for solvated AIMS initial conditions

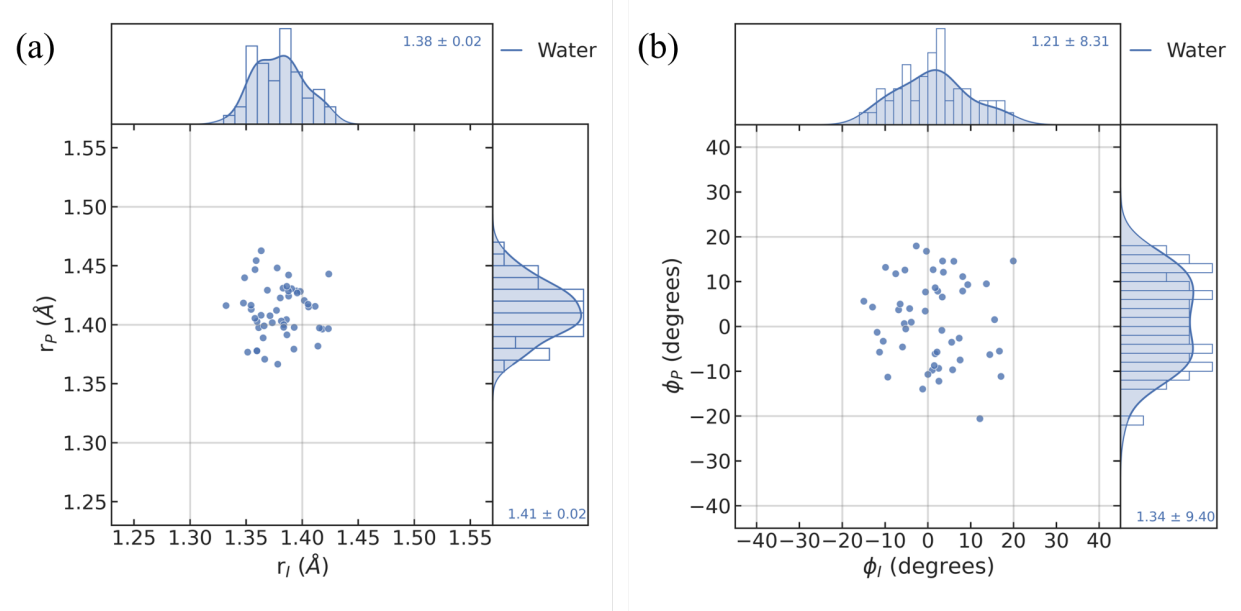

Figure S8: As in Figure S7, but restricted to initial conditions that were used for the AIMS dynamics in explicit water at 300K.

IX. Electronic effects of solvation

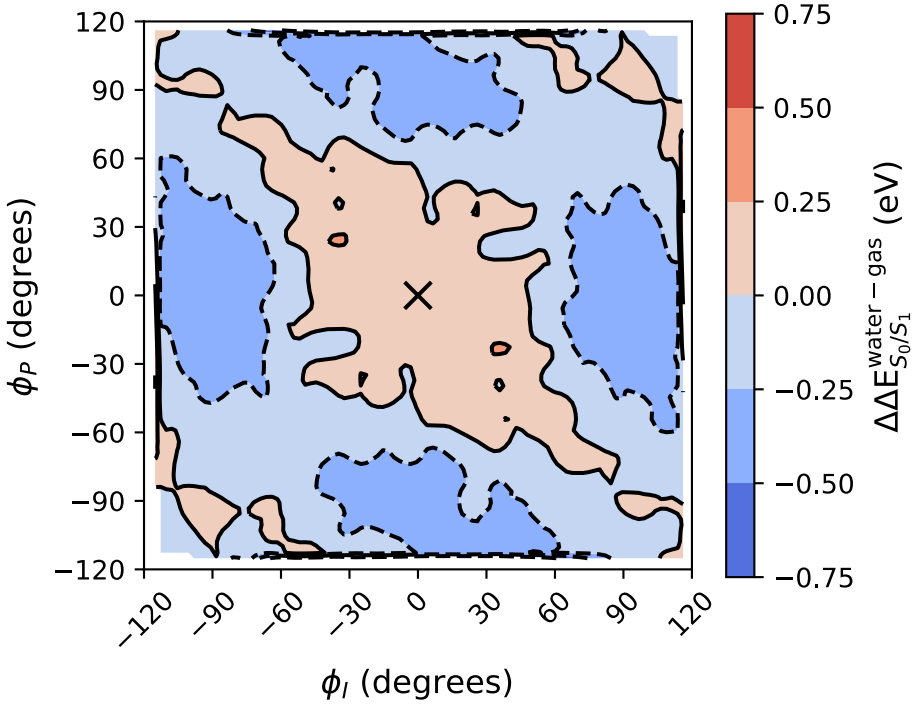

Figure S9: Difference between S_0/S_1 energy gaps in water (Figure 6a) and in gas-phase (Figure 6b) systems. Gas-phase energies correspond to umbrella-sampled solvated structures after removing the solvent around the chromophore. The average dihedral angles and energy gaps were plotted for each 10° window from the umbrella sampling, and cubic interpolation was performed between these points. The zero point (marked with an "X") corresponds to the planar structure.

X. Excited-state population decay of red-shifted and blue-shifted initial conditions

Based on the ratio of I- and P-twisted pathways taken by red- and blue-shifted ICs (Table S4), the excitation wavelength may impact the subsequent deactivation path. An increased I-twisted/P-twisted ratio for blue-shifted ICs, relative to red-shifted ICs, explains the faster population transfer observed for blue-shifted ICs when compared to the population transfer of their red-shifted counterparts. However, there is only limited sampling to support this claim of wavelength-dependent branching ratios, and further investigations are necessary to establish and explain the origin of this difference.

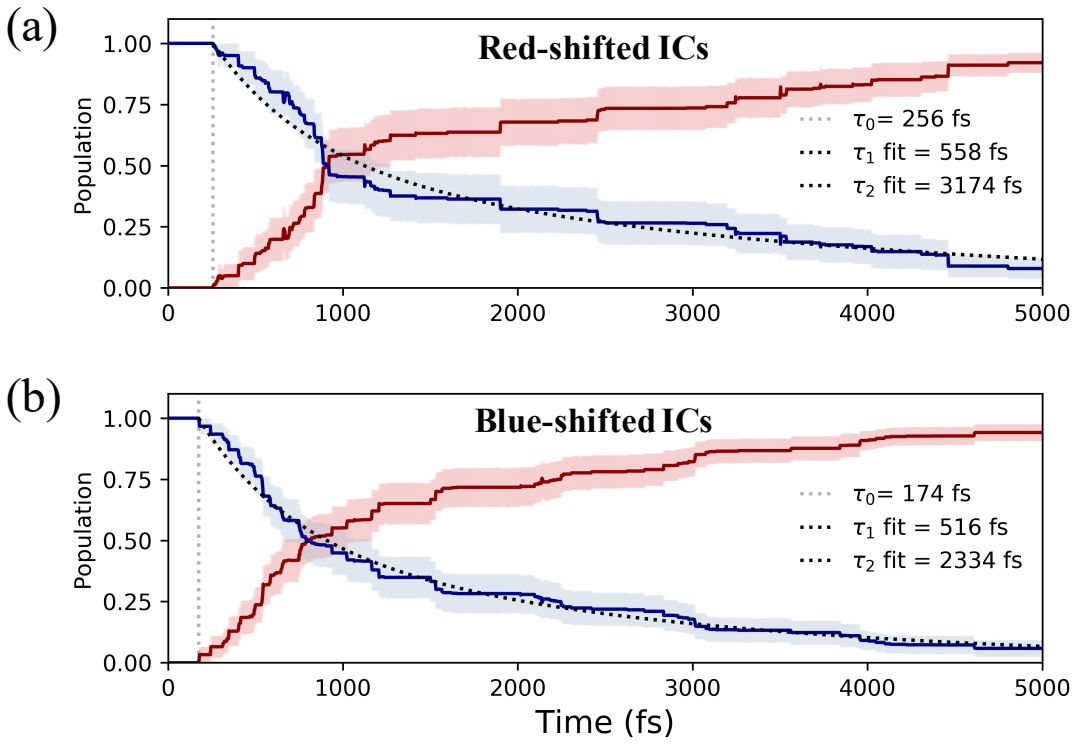

Figure S10: Ground-state (red) and excited-state (blue) population of $HBDI^-$ in water for (a) red-shifted initial conditions (S_0/S_1 excitation energy < 2.84 eV) and (b) blue-shifted initial conditions (S_0/S_1 excitation energy > 2.84 eV). Populations are averaged across all initial conditions for each species. Solid lines represent the average populations for each state. The vertical, gray dotted line represents the time at which population transfer begins (τ_0). The black dotted line is the delayed bi-exponential fit (consisting of τ_1 and τ_2 components) to the S_1 population decay. Transparent lines represent the error obtained from bootstrapping analysis.

XI. Flapping angle of $HBDI^-$ during AIMS dynamics

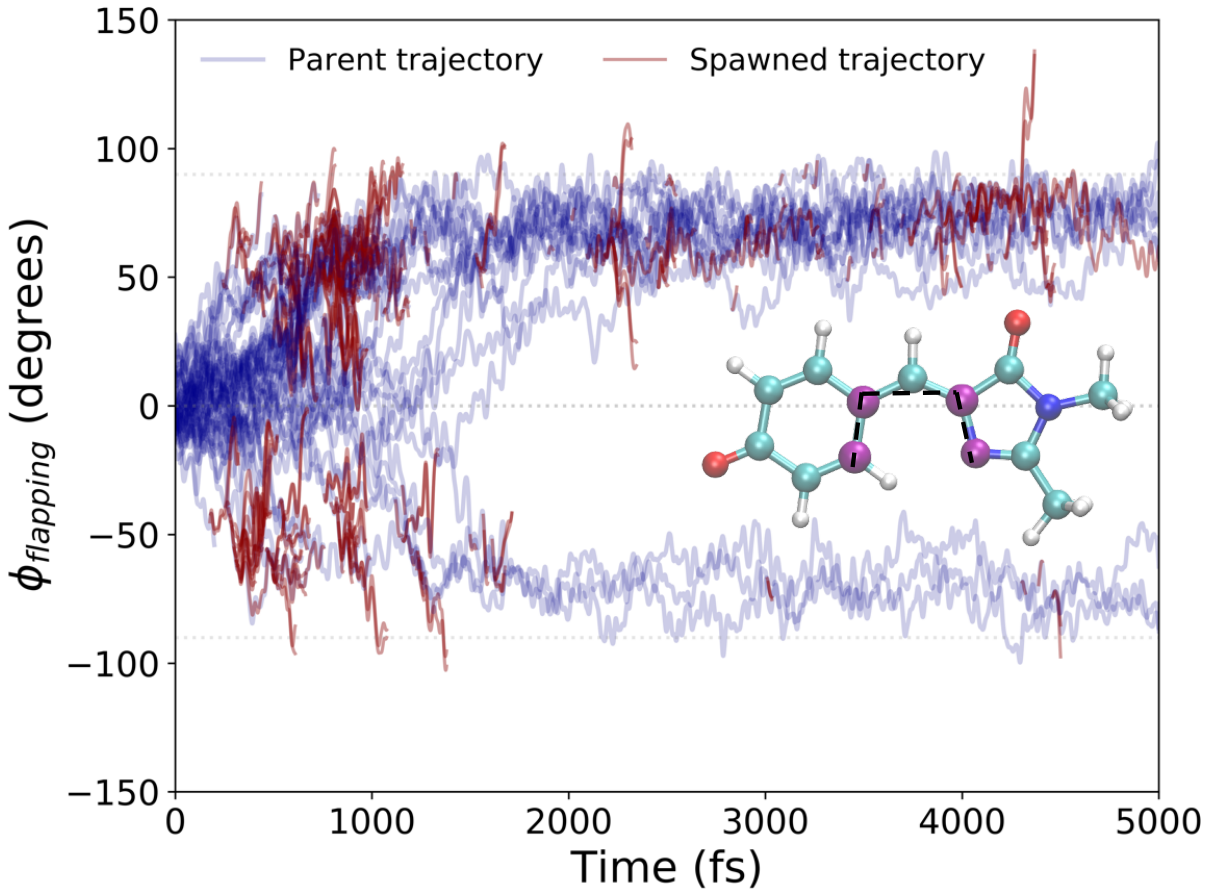

Figure S11: Flapping angle (ϕ_{flapping}) between the I- and P-rings during AIMS dynamics of $HBDI^-$ in water. Blue lines represent parent TBFs, and red lines represent spawned TBFs. Atoms involved in calculating the flapping angle are highlighted in purple, and the flapping angle is defined as the dihedral angle illustrated by the inset.

XII. Relative population transfer of HBDI⁻ spawning events

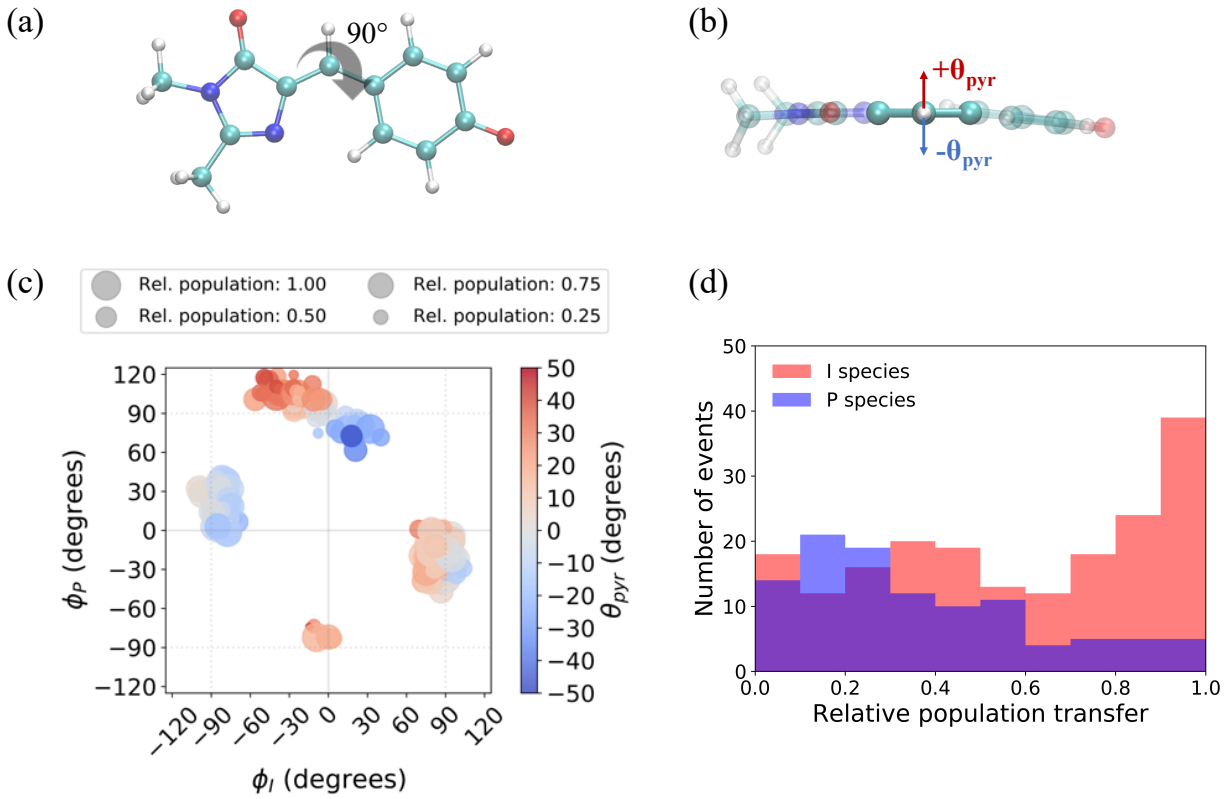

Figure S12: (a) Visual of the 90° rotation of HBDI⁻ that leads to the orientation in (b), which illustrates positive and negative θ_{pyr} angles. (c) Relative population transfer and pyramidalization angle associated with the bridge carbon atom for spawned geometries of HBDI⁻ in water from parent TBFs. ϕ_I and ϕ_P dihedral angles correspond to geometries upon entering a spawning region. Relative population transfer is defined by the fraction of incoming S_1 population transferred to S_0 relative to the S_1 population upon entering the spawning region. (d) Relative population transfer distributions of I- and P-spawning events in water.

XIII. Dihedral angle distribution for spawned $HBDI^-$ geometries

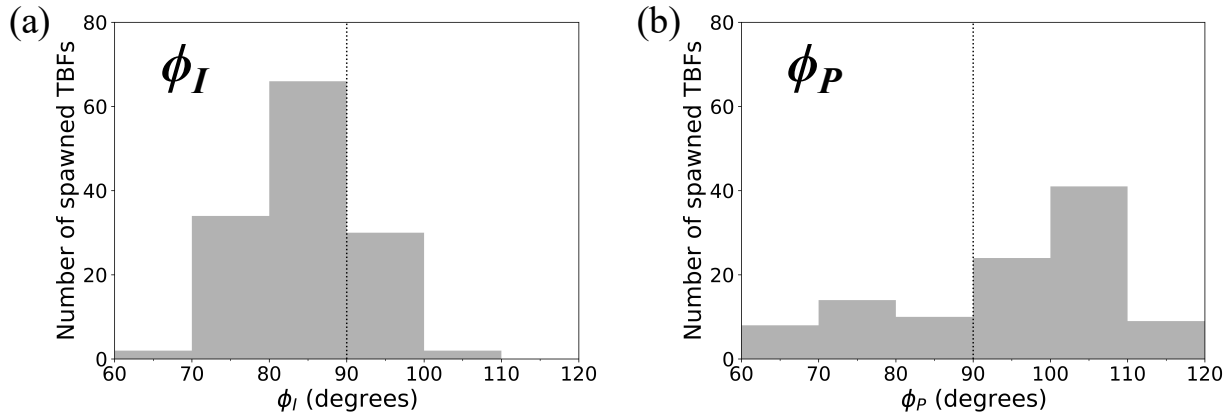

Figure S13: Dihedral angle distribution for spawned geometries of $HBDI^-$ in water (from S_1 to S_0). (a) ϕ_I dihedral angle distribution for TBFs of initial conditions that undergo I-deactivation. (b) ϕ_P dihedral angle distribution for TBFs of initial conditions that undergo P-deactivation.

XIV. Photoproducts of $HBDI^-$

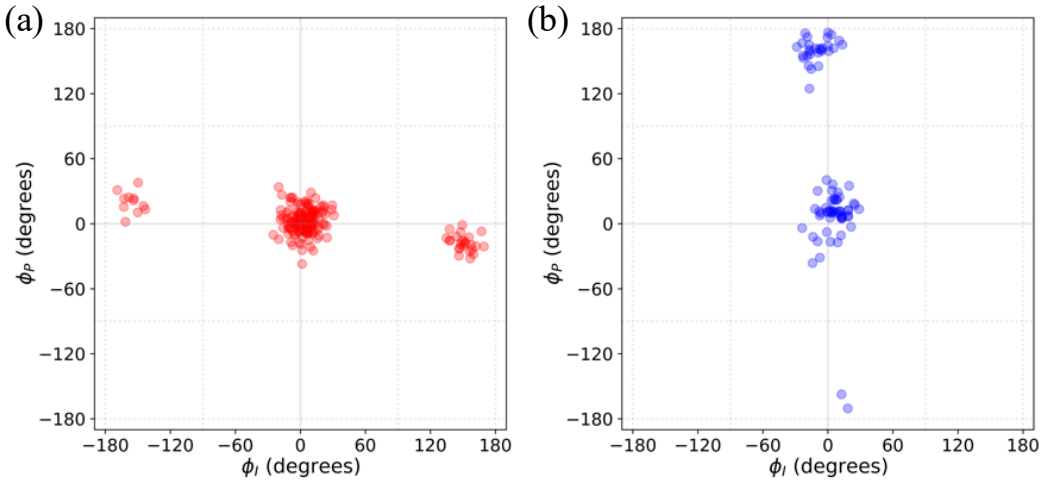

Figure S14: Photoproducts of $HBDI^-$ initial conditions, following 500 fs of ground-state QM/MM-MD simulations for child TBFs spawned on S_0. Photoproducts are shown for spawned geometries reached via (a) I-twisted and (b) P-twisted deactivation.

XV. Comparison of experimental and theoretical fluorescence maxima

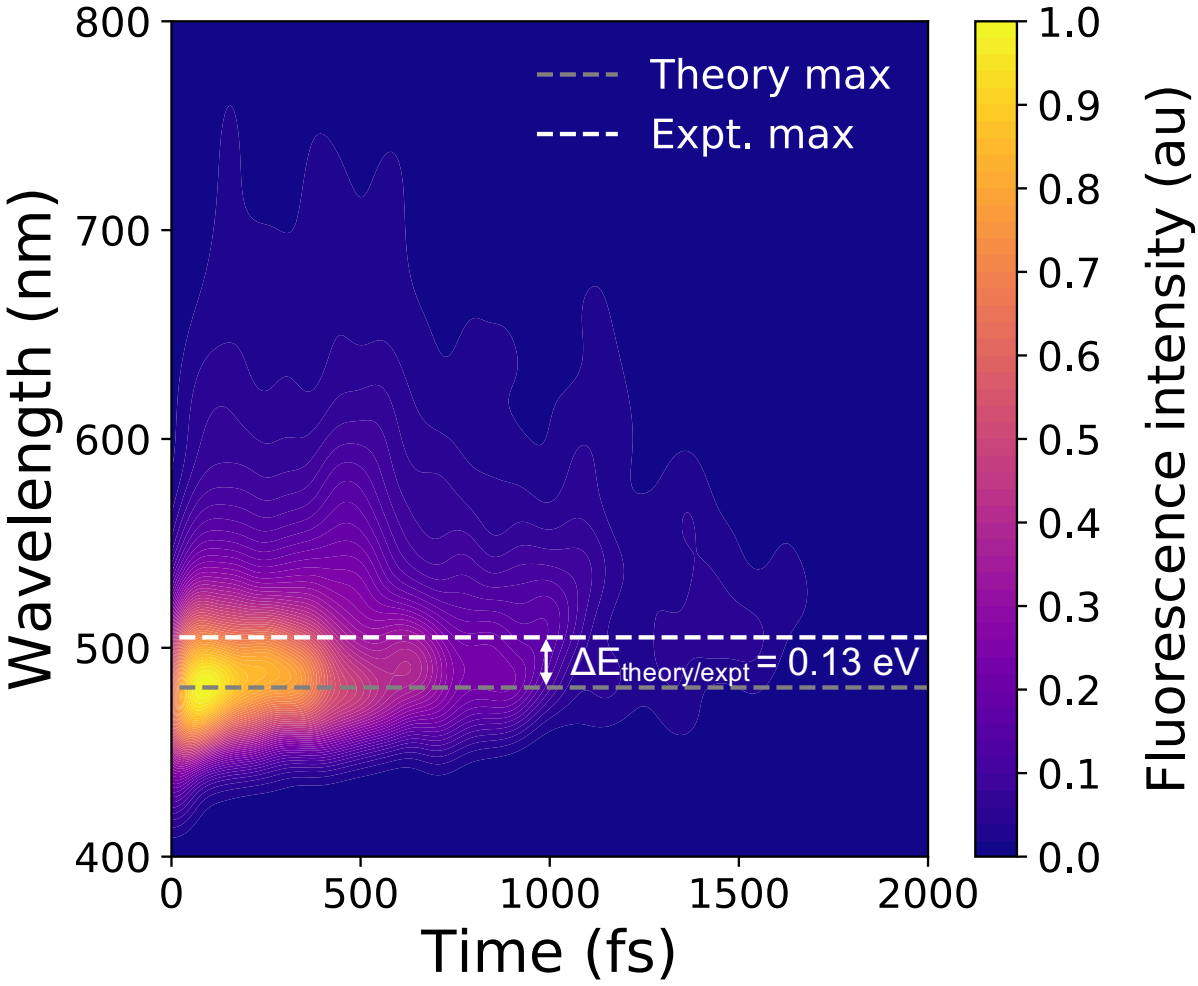

Figure S15: Fluorescence maxima of solvated HBDI⁻ from theory and experiment.[4] The theory spectrum consists of data from all fifty initial conditions. Based on this energy gap, the theory spectra were shifted by 0.13 eV to align the two maxima for analysis purposes.

XVI. Oscillator strength as a function of twisting angles

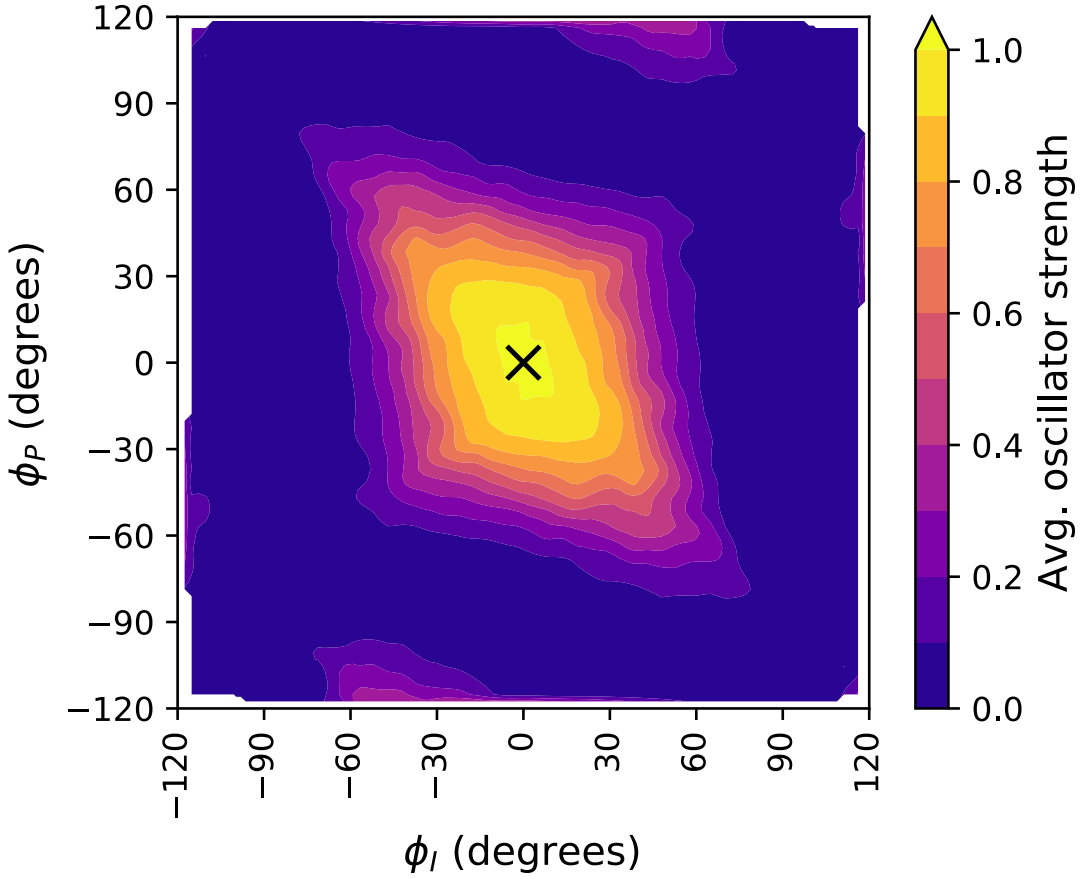

Figure S16: Oscillator strength of aqueous $HBDI^-$ as a function of twisting along ϕ_I and ϕ_P dihedral angles. Data is obtained from average dihedral angles and oscillator strengths recorded for 10° umbrella sampling windows on S_1. The "X" marker at the origin represents the point of complete planarity with respect to the ϕ_I and ϕ_P dihedral angles.

XVII. Geometric parameters of critical points in water

Table S1: Key geometric parameters for representative α(0.67)-SA3-CASSCF(4,3)/6-31G* critical points of $HBDI^-$ in water.

	r_I (Å)	r_P (Å)	ϕ_I (degrees)	ϕ_P (degrees)	θ_{pyr} (degrees)
S_0 minimum	1.38	1.41	4.28	11.67	1.97
MECI-I	1.45	1.41	84.31	4.31	14.39
MECI-P	1.43	1.48	17.03	72.68	-34.23

XVIII. Comparison of S_0/S_1 energy gap across multiple complete active space methods

Table S2: Difference between S_0 and S_1 electronic state energies for geometries used to benchmark α-CASSCF(4,3) in water. The FC geometry is optimized on S_0, and all other geometries are optimized on S_1. The α(0.67)-SA3-CASSCF(4,3) method was used for optimization. XMS-CASPT2(4,3) and SA3-CASSCF(4,3) single point energy calculations were run on the optimized α-CASSCF geometries. A 6-31G* basis set was used for all methods.

	α(0.67)-SA3-CASSCF(4,3) (eV)	**XMS-CASPT2(4,3) (eV)**	**SA3-CASSCF(4,3) (eV)**
FC	2.90	2.90	4.33
Planar	2.92	2.92	4.36
I15 / P15	2.54 / 2.62	2.55 / 2.61	3.80 / 3.90
I30 / P30	2.28 / 2.45	2.31 / 2.45	3.40 / 3.65
I45 / P45	1.83 / 2.08	1.90 / 2.13	2.73 / 3.11
I60 / P60	1.25 / 1.42	1.36 / 1.56	1.86 / 2.11
I75 / P75	0.45 / 0.95	0.63 / 1.24	0.66 / 1.42
I90 / P90	0.09 / 0.86	0.36 / 1.24	0.13 / 1.28

XIX. Oscillator strength of geometries used to benchmark α-CASSCF

Table S3: Oscillator strength of $S_0 \rightarrow S_1$ electronic transitions for geometries used to benchmark α-CASSCF(4,3) in water. The FC geometry is optimized on S_0, and all other geometries are optimized on S_1. The α(0.67)-SA3-CASSCF(4,3)/6-31G* method and basis set were used for optimization.

	Oscillator strength, $S_0 \rightarrow S_1$ (a.u.)	**Energy gap, $S_0 \rightarrow S_1$ (eV)**
FC	1.13	2.90
Planar	1.15	2.92
I15 / P15	1.01 / 1.08	2.54 / 2.62
I30 / P30	0.80 / 0.96	2.28 / 2.45
I45 / P45	0.53 / 0.67	1.83 / 2.08
I60 / P60	0.30 / 0.28	1.25 / 1.42
I75 / P75	0.08 / 0.07	0.45 / 0.95
I90 / P90	0.00 / 0.01	0.09 / 0.86

XX. Transition dipole moments of α-CASSCF compared to EOM-CCSD

The fluorescence spectrum is calculated using the transition dipole moment between the S_0 and S_1 electronic states, $\mu_{S0/S1}$. While α-CASSCF scales energy, the CASSCF wavefunction remains unaffected. Therefore, $\mu_{S0/S1}$ is identical for α-CASSCF and CASSCF. For comparison, we calculated the transition dipole moments of I- and P-twisted geometries using the equation-of-motion coupled cluster method with single and double excitations (EOM-CCSD).

Table S4: Squared transition dipole moment (in atomic units) associated with the $S_0 \rightarrow S_1$ electronic transitions for geometries used to benchmark α-CASSCF(4,3) in water. All geometries were optimized on S_1 at the α(0.67)-SA3-CASSCF(4,3)/6-31G* level. EOM-CCSD transition dipole moments are computed using the aug-cc-pVDZ basis set.

	$\lvert\mu_{S0/S1}\rvert^2$	
	α-CASSCF/6-31G*	**EOM-CCSD/aug-cc-pVDZ**
Planar	16.76	15.68
I15 / P15	16.27 / 16.78	15.91 / 15.71
I30 / P30	14.30 / 15.96	14.76 / 14.53
I45 / P45	11.87 / 13.07	12.07 / 11.37
I60 / P60	9.83 / 8.13	8.29 / 5.52
I75 / P75	7.69 / 2.97	2.55 / 1.31
I90 / P90	1.39 / 0.33	0.01 / 0.12

XXI. Geometric and electronic contributions to the blue-shifted absorption spectrum upon solvation

To isolate the geometric and electronic perturbations induced by explicit solvation, we observe the shift of the absorption spectrum based on whether $HBDI^-$ is isolated or surrounded by water. In particular, a comparison of the QM/MM-MD absorption spectrum of aqueous $HBDI^-$ to that generated by the same $HBDI^-$ configurations but in isolation allows us to directly gauge the electronic effects of solvation. Similarly, the spectral shift obtained by comparing the absorption spectrum of the solvent-removed configurations to that from a gas-phase QM/MM-MD sampling (Figure S7) enables us to isolate geometric effects of the solvent.

Table S5: Change in the absorption maximum of $HBDI^-$ as a function of the chromophore's environment. The calculated ΔE_{abs} from ground-state QM/MM-MD sampling, either in the gas-phase or in water, is compared to the ΔE_{abs} calculated for configurations of aqueous $HBDI^-$ following the removal of the solvent. The same solvent-removed samples are used for comparison to gas-phase and water QM/MM-MD samples. However, since α is a scaling parameter, choosing an α value consistent with the QM/MM-MD sampling procedure is necessary to avoid spurious energy shifts upon comparison.

	ΔE_{abs} maximum: QM/MM-MD (eV)	**ΔE_{abs} maximum: Solvent removed (eV)**	**$\Delta\Delta E_{abs}$ maximum**
Gas (α=0.64)	2.56 ± 0.07	2.53 ± 0.07	0.03
Water (α=0.67)	2.84 ± 0.09	2.65 ± 0.08	0.19

XXII. Photoproducts of red-shifted and blue-shifted initial conditions

Table S6: Classifications for red-shifted (S_0/S_1 excitation energy < 2.84 eV) and blue-shifted (S_0/S_1 excitation energy > 2.84 eV) initial conditions used for AIMS simulations of $HBDI^-$ in water. Each initial condition is classified based on whether rotation around ϕ_I or ϕ_P is dominant on S_1. The I/P ratio average and standard deviation for red-shifted and blue-shifted initial conditions are based on a bootstrapping analysis using 1000 bootstrapping samples.

	Initial conditions	I-products	P-products	I/P ratio
Red-shifted	20	12	8	1.7 ± 1.1
Blue-shifted	30	21	9	2.7 ± 1.6

XXIII. Classifications for TBF photoproducts

Table S7: Classifications for I- and P-twisted photoproducts, based on the configuration of spawned geometries after 500 fs of ground-state QM/MM-MD. A threshold of 120° is used to determine whether a *Z*-1 product (less than 120°) or an isomerized product (greater than 120°) is generated. The *Z*-1 product represents a *Z*-isomer of $HBDI^-$ that is not the result of *Z/Z* isomerization.

	Total spawns	***Z*-1 products**	**Isomerized products**
I-channel	181	145	36
P-channel	83	52	31

References

1. J. W. Park and T. Shiozaki, *J Chem Theory Comput*, 2017, **13**, 3676-3683.
2. A. Toniolo, G. Granucci and T. J. Martínez, *J Phys Chem A*, 2003, **107**, 3822-3830.
3. A. Toniolo, S. Olsen, L. Manohar and T. J. Martínez, *Faraday Discuss*, 2004, **127**, 149-163.
4. M. A. Taylor, L. Zhu, N. D. Rozanov, K. T. Stout, C. Chen and C. Fang, *Phys Chem Chem Phys*, 2019, **21**, 9728-9739.